

# Experimental characterization of coherent magnetization transport in a one-dimensional spin system

Chandrasekhar Ramanathan<sup>1</sup>, Paola Cappellaro<sup>2</sup>,  
Lorenza Viola<sup>1</sup>, David G. Cory<sup>3,4</sup>

E-mail: `sekhar.ramanathan@dartmouth.edu`

<sup>1</sup>Department of Physics and Astronomy, Dartmouth College, Hanover, NH 03755, USA

<sup>2</sup>Department of Nuclear Science and Engineering, Massachusetts Institute of Technology, Cambridge, MA 02139, USA

<sup>3</sup>Department of Chemistry and Institute for Quantum Computing, University of Waterloo, Waterloo ON N2L 3G1, Canada

<sup>4</sup>Perimeter Institute for Theoretical Physics, Waterloo, ON N2L 2Y5, Canada

**Abstract.** We experimentally characterize the non-equilibrium, room-temperature magnetization dynamics of a spin chain evolving under an effective double-quantum Hamiltonian. We show that the Liouville space operators corresponding to the magnetization and the two-spin correlations evolve 90 degrees out of phase with each other, and drive the transport dynamics. For a nearest-neighbor-coupled  $N$ -spin chain, the dynamics are found to be restricted to a Liouville operator space whose dimension scales only as  $N^2$ , leading to a slow growth of multi-spin correlations. Even though long-range couplings are present in the real system, we find excellent agreement between the analytical predictions and our experimental results, confirming that leakage out of the restricted Liouville space is slow on the timescales investigated. Our results indicate that the group velocity of the magnetization is  $6.04 \pm 0.38 \mu\text{m/s}$ , corresponding to a coherent transport over  $N \approx 26$  spins on the experimental timescale. As the double-quantum Hamiltonian is related to the standard one-dimensional XX Hamiltonian by a similarity transform, our results can be directly extended to XX quantum spin chains, which have been extensively studied in the context of both quantum magnetism and quantum information processing.

PACS numbers: 03.67.Hk, 75.10.Pq, 76.90.+d

## 1. Introduction

Solid-state spin systems provide an attractive test-bed to study both equilibrium and non-equilibrium quantum many-body dynamics, and have recently emerged as a promising platform for quantum simulation [1, 2]. One-dimensional (1D) spin systems, in particular, are of special interest as they connect to an important class of problems in condensed-matter physics [3], and have been suggested as quantum wires to coherently transfer quantum information across distant nodes in a quantum computer and distributed quantum architectures [4, 5]. Transport properties, and magnetization transport in particular, have been extensively investigated theoretically by both the condensed-matter community and more recently in the context of spintronics and emerging nano-device applications [6].

The class of 1D spin-1/2 XY Hamiltonians [7, 8, 9], which are exactly solvable via a Jordan-Wigner mapping onto a system of non-interacting spinless fermions, play an archetypal role in condensed-matter physics. In this case, a local magnetic disturbance is known to propagate down the chain scatter-free with a constant velocity (*ballistic transport*), rather than diffusively spreading from the site of the disturbance and eventually decaying (*diffusive transport*). From a quantum communication perspective, the mapping to free fermions has proved crucial to also allow a quantum state to be transported down the chain — which thus acts as a quantum conduit or channel (see for example [10] for a recent review). While at zero temperature, within linear response theory, integrable quantum models are typically associated with ballistic transport, a coexistence with and/or crossover to diffusive behavior may be possible more generally, for instance in the presence of non-local conserved quantities [11] or of couplings to an environment [12, 13, 14]. Despite significant progress, a satisfactory understanding of the conditions leading to ballistic versus diffusive transport is as yet lacking, with a number of unresolved questions remaining, in particular, in relation to the impact of finite and infinite temperatures [15], the role of non-integrability, and its interplay with frustration [16, 17]. As a result, experimentally characterizing the transport properties and physical mechanisms in low-dimensional spin systems remains important from both fundamental and applied standpoints.

The long coherence times afforded by nuclear spins and the ability to access a large Hilbert space, in conjunction with the superb level of control available over spin degrees of freedom, make solid-state nuclear magnetic resonance (NMR) an excellent setting for exploring the coherent dynamics of a (nearly) isolated quantum many-body system [1, 18, 19, 20] as well as the statistical physics of equilibrating spin systems [21, 22, 23]. In this work, we employ solid-state NMR techniques to characterize the room-temperature magnetization dynamics of a (quasi) 1D spin system during coherent evolution under an effective Double Quantum (DQ) Hamiltonian, which is directly related to the isotropic XY (XX henceforth) Hamiltonian by a similarity transformation. In particular, we find that the experimental results are in very good agreement with those predicted by the free-fermionic solutions, indicating that integrability-breaking perturbations (due to

longer range couplings) have negligible effect on the timescale of the experiments, and enabling us to calculate the transport velocity of the magnetization. This is in marked contrast to the diffusive behavior observed under the dipolar Hamiltonian in previous experiments on 3D spin networks [24, 25], where spin diffusion arises from unitary dynamics under the high-field (secular) dipolar Hamiltonian. While experimentally the high degree of isolation from the surrounding environment during evolution was demonstrated by the observation of “polarization echoes” upon reversing the sign of the dipolar Hamiltonian [26], quantum chaoticity was explicitly invoked theoretically as a mechanism for diffusion [27, 28].

Beside providing additional insight into the mechanisms underlying coherent transport in *isolated 1D many-body quantum systems*, in the context of quantum information transport it is important to stress that the nuclear spin chains we study here are initially in a *highly mixed* quantum state. The importance of relaxing initialization constraints is being increasingly appreciated within the quantum communication community (see in particular [29] and references therein). We thus expect this study to also be of direct relevance to a number of other quantum platforms where mixed-state spin chains are naturally encountered, such as phosphorus defects in silicon nanowires [30], quantum dots [31, 32], molecular semiconductors [33] and solid-state defects in diamond or silicon carbide [34, 35].

## 2. Experimental Methods and Results

The  $^{19}\text{F}$  spins in a crystal of fluorapatite (FAP –  $\text{Ca}_5(\text{PO}_4)_3\text{F}$ ) have long been used to experimentally approximate a nearest-neighbor coupled 1D spin system (see for example [36, 37, 38, 39, 40]). In a 3D lattice of dipolar-coupled nuclear spins, every pair of spins is coupled with an interaction strength (between spin  $j$  and spin  $\ell$ )  $d_{j\ell} = (\mu_0/16\pi)(\gamma^2\hbar/r_{j\ell}^3)(1 - 3\cos^2\theta_{j\ell})$  [41], where  $\gamma$  is the gyromagnetic ratio of fluorine,  $r_{j\ell}$  is the distance between nucleus  $j$  and  $\ell$ , and  $\theta_{j\ell}$  is the angle between  $\vec{r}_{j\ell}$  and the  $z$ -axis (along which the external magnetic field is applied). The geometry of the spin system is reflected in the distribution of the  $d_{j\ell}$  couplings. In FAP, the  $^{19}\text{F}$  nuclei form linear chains along the  $c$ -axis, each one surrounded by six other chains. The distance between two intra-chain  $^{19}\text{F}$  nuclei is  $r = 3.442 \text{ \AA}$  whereas the distance between two cross-chain  $^{19}\text{F}$  nuclei is  $R = 9.367 \text{ \AA}$ . The largest ratio between the strongest intra- and cross-chain couplings ( $\approx 40$ ) is obtained when the crystalline  $c$ -axis is oriented parallel to the external field. In this orientation, the fluorine spins may be treated as a collection of many identical 1D chains with only nearest-neighbor (NN) couplings, with a coupling strength  $d \equiv (\mu_0/8\pi)\gamma^2/r^3 = 8.17 \times 10^3 \text{ rad/s}$ .

In this NN approximation, the high-field secular dipolar Hamiltonian of a single chain is given by  $\mathcal{H}_{\text{Dip}} = \frac{1}{2} \sum_{i=1}^{N-1} d (3\sigma_i^z \sigma_{i+1}^z - \vec{\sigma}_i \cdot \vec{\sigma}_{i+1})$ , where  $\sigma^\alpha$  ( $\alpha = x, y, z$ ) are the Pauli operators. Starting from  $\mathcal{H}_{\text{Dip}}$  and using suitable multiple-pulse sequences [43, 44],

we can experimentally implement an effective DQ Hamiltonian, given by

$$\mathcal{H}_{\text{DQ}} = \frac{1}{2} \sum_i^{N-1} d (\sigma_i^x \sigma_{i+1}^x - \sigma_i^y \sigma_{i+1}^y). \quad (1)$$

Formally, the DQ Hamiltonian is related to the standard XX Hamiltonian by the similarity transformation  $U_{\text{DQ}}^{\text{XX}} = \exp(-i\pi/2 \sum_i \sigma_x^i)$ , where the sum is restricted to either even or odd spins. While  $I_z \propto \sum_i I_z^i$  is conserved under the XX Hamiltonian, the corresponding conserved quantity under the DQ Hamiltonian is  $\tilde{I}_z \propto U_{\text{DQ}}^{\text{XX}} I_z U_{\text{DQ}}^{\text{XX}\dagger}$ . This results in the inversion of sign of the local magnetic disturbance at every alternate site as it moves down the chain, as will be seen later (see Figure 6).

In order to implement the DQ Hamiltonian, we used a standard 8-pulse sequence applied on-resonance to the  $^{19}\text{F}$  Larmor frequency [43]. This 8-pulse sequence,  $\mathbf{S} = \mathbf{C} \cdot \bar{\mathbf{C}} \cdot \bar{\mathbf{C}} \cdot \mathbf{C}$ , may be understood in terms of a simpler 2-pulse cycle ( $\mathbf{C}$ , and its time-reversed version  $\bar{\mathbf{C}}$ ), which also simulates the DQ Hamiltonian. The primitive pulse cycle is given by  $\mathbf{C} = [\frac{\Delta}{2} X \Delta' X \frac{\Delta}{2}]$ , where  $\Delta' = 2\Delta + w$ ,  $\Delta$  is the delay between pulses and  $w$  is the width the  $\pi/2$  pulse (denoted by  $X$ ), applied about the  $x$ -axis. The dynamics in the presence of the pulse sequence can be expressed in terms of a time-independent effective Hamiltonian  $\bar{\mathcal{H}}_{\text{DQ}}$ ,

$$U_{\text{MQ}}^x(t) = \mathcal{T} \exp \left( -i \int_0^t [\mathcal{H}_{\text{dip}} + \mathcal{H}_{\text{rf}}^x(s)] ds \right) = e^{-i\bar{\mathcal{H}}_{\text{DQ}} t}, \quad (2)$$

where  $\mathcal{T}$  denotes time-ordering operator,  $\hbar = 1$ , and  $\mathcal{H}_{\text{rf}}^x(t)$  is the time-dependent Hamiltonian describing the rf-pulses along the  $x$ -axis. This sequence implements the Hamiltonian of Eq. (1) to the lowest order in an average Hamiltonian theory sense [45].

In an inductively detected NMR experiment where we measure quadrature signals from the  $x$  and  $y$  components of the precessing magnetization, the observed signal is  $S(t) = \zeta \langle \sigma^-(t) \rangle = \zeta \text{Tr} \{ \sigma^- \rho(t) \}$ , where  $\sigma^- = \sum_j \sigma_j^- = \sum_j (\sigma_j^x - i\sigma_j^y)/2$ , and  $\zeta$  is a proportionality constant. The only terms in  $\rho(t)$  that yield a non-zero trace, and therefore contribute to  $S(t)$ , are angular momentum operators such as  $\sigma_j^+$ , which are single-spin, so-called ‘‘single-quantum coherences’’ in the language of multiple-quantum (MQ) NMR [42]. In a standard MQ experiment that is used to characterize the many-spin dynamics of a nuclear spin system, the uncorrelated thermal initial states of the spins are allowed to evolve under a Hamiltonian such as the DQ Hamiltonian that generates the multi-spin dynamics. The multi-spin character of the states is indirectly encoded by a collective rotation of the spins and the DQ evolution is then reversed to convert the many-spin states back to single spin terms that can be detected.

Our experiments were performed at room temperature in a 7T vertical bore NMR magnet on a single FAp crystal with its  $c$ -axis aligned to the external field. The measured  $T_1$  of the fluorine spins was 300 s (many orders of magnitude larger than the timescales explored experimentally here). The length of the  $\pi/2$  pulse used was  $w = 1.06 \mu\text{s}$  and  $\Delta = 2.9 \mu\text{s}$ . The *thermal (equilibrium) state* of the spins in high field and high temperature is highly mixed, and is given by  $\rho_{\text{th}} \approx \mathbf{1} - \epsilon \sum_i \sigma_z^i$ , where  $\epsilon \sim 10^{-5} \ll 1$ . The identity is unchanged under unitary transformations, and does not contribute to the

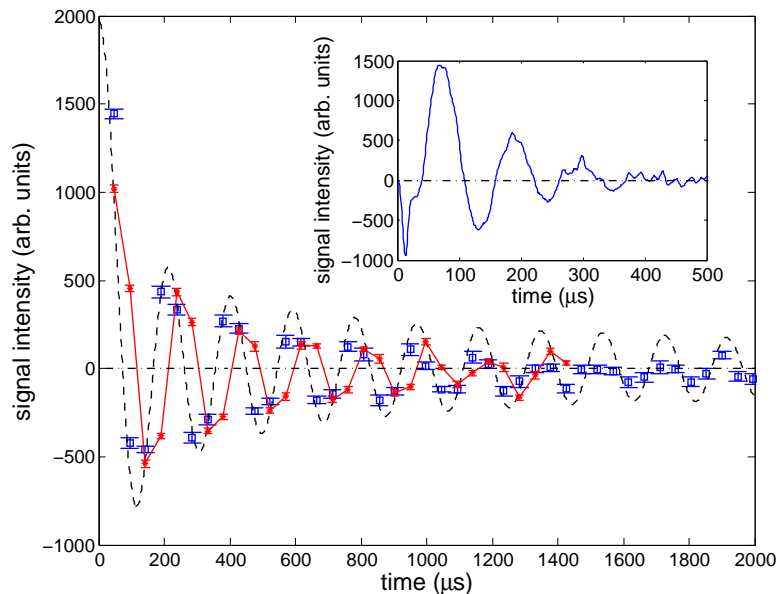


**Figure 1.** Evolution of the thermal initial state under  $\mathcal{H}_{\text{DQ}}$ . The blue squares correspond to the collective magnetization ( $\sum_i \sigma_z^i$ ) and the red asterisks to the two-spin correlations ( $\sum_i (\sigma_x^i \sigma_y^{i+1} + \sigma_y^i \sigma_x^{i+1})$ ). The dashed black line is the best fit of the observed magnetization to the analytical model described later. The solid red line is a guide to the eye. The inset shows the NMR FID of FAp.

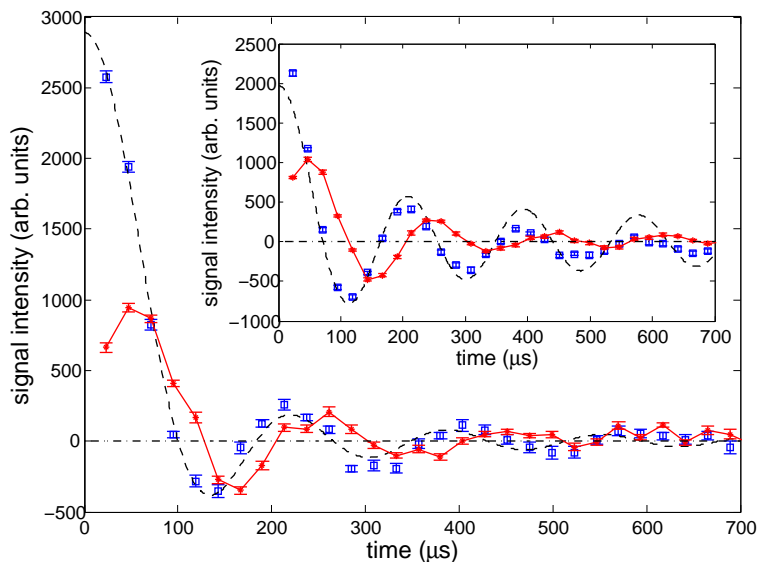
signal  $S(t)$ . Thus, it is only the *deviation* of the density operator from the identity that gives rise to an observable signal. The constant  $\epsilon$  then becomes a scaling parameter and its value does not affect the details of the experiment (as long as the high temperature approximation remains valid).

Figure 1 shows the observed evolution of the collective magnetization ( $\propto \sum_i \sigma_z^i$  – blue squares) and the two-spin correlations ( $\propto \sum_i (\sigma_x^i \sigma_y^{i+1} + \sigma_y^i \sigma_x^{i+1})$  – red asterisks) under  $\mathcal{H}_{\text{DQ}}$ , starting from  $\rho_{\text{th}}$ . The error bars were estimated from the standard deviation of a signal-free region of the time-domain data. The evolution time was incremented by increasing the number of cycles from 1 to 40 (30 in the two-spin correlation readout).

In contrast to typical NMR experiments which involve the DQ Hamiltonian [43], no evolution reversal was performed before signal detection in our experiments. In order to minimize receiver dead-time effects, a solid echo was used to read out the (single-spin) magnetization terms. The two-spin terms were read out using a  $\pi/4$  pulse to generate a dipolar echo (with an appropriate phase cycle). The combination of a  $\pi/4$  pulse followed by evolution under the dipolar Hamiltonian refocuses a portion of the two-spin correlations back to single-spin coherences that can then be detected [41]. The importance of the single-spin and two-spin operators in driving the transport dynamics can be seen from the following equations (the short time dynamics are further discussed in Appendix B):

$$\frac{d}{dt} \sigma_1^z = \frac{id}{2} (\sigma_1^x \sigma_2^y + \sigma_1^y \sigma_2^x), \quad \frac{d}{dt} (\sigma_1^x \sigma_2^y + \sigma_1^y \sigma_2^x) = -d \sigma_2^z + 3 \text{ spin terms.} \quad (3)$$

As a result, the single-spin and two-spin terms are observed to evolve 90 degrees out



**Figure 2.** Evolution of the end-polarized initial state under  $\mathcal{H}_{\text{DQ}}$ . The blue squares correspond to  $\sum_i \sigma_z^i$ , while the red asterisks correspond to  $\sum_i (\sigma_x^i \sigma_y^{i+1} + \sigma_y^i \sigma_x^{i+1})$ . Inset shows the 4-pulse experiment on the thermal initial state. The dashed black lines are the best fits of the magnetization dynamics to the analytical model.

of phase with each other during DQ evolution. The inset shows the observed NMR Free Induction Decay (FID), which corresponds to the evolution of  $\sum_i \sigma_x^i$  under  $\mathcal{H}_{\text{Dip}}$ . While the FID decays in about  $350 \mu\text{s}$ , due to the creation of multi-spin correlations [18], the magnetization oscillations persist for up to  $\approx 1.5 \text{ ms}$  under  $\mathcal{H}_{\text{DQ}}$ , indicating that high-order spin correlations develop quite slowly [46].

It is also possible to experimentally prepare initial states of the form  $\rho_{1N} \approx \mathbf{1} - \epsilon(\sigma_1^z + \sigma_N^z)$  [47], in which the polarization is localized at the ends of the chain. We call this the *end-polarized state*. Figure 2 shows the DQ evolution observed for  $\rho_{1N}$ . Here, we implemented  $\mathcal{H}_{\text{DQ}}$  using the first 4 pulses of the above sequence ( $\mathbb{C} \cdot \bar{\mathbb{C}}$ ) to achieve better temporal sampling of the signal, though this introduces first-order errors in the resulting average Hamiltonian. The alternating sign of the local magnetization during spin transport of the end-polarized state results in a rapid attenuation of the amplitudes of the observed signal (the 8-pulse version of the experiment is included in Appendix A). For comparison, the inset shows the 4-pulse version of the thermal state experiment.

### 3. Theoretical Analysis and Interpretation

#### 3.1. Fermionic Model

Both the NN XX [7] and NN DQ [47, 48] Hamiltonians are well known to be analytically solvable in 1D, by means of a Jordan-Wigner mapping onto a system of free fermions. We invoke this mapping to interpret the experimental results. Starting from an end-

polarized initial state  $\rho_j = \mathbf{1} - \sigma_j^z$ , we once again take note of the fact that the identity does not evolve, and focus our attention on the deviation term  $\sigma_j^z$ . The deviation density operator at time  $t$  under the DQ Hamiltonian is given by [47, 49]:

$$\rho_j^{\text{DQ}}(t) = \frac{1}{N+1} \sum_{k,h=1}^N \sin(kj) \sin(hj) \times \left[ \left( a_k^\dagger a_h + a_h^\dagger a_k \right) \cos \psi_{kh}(t) - i \left( a_k^\dagger a_h^\dagger - a_h a_k \right) \sin \psi_{kh}(t) \right], \quad (4)$$

where  $a_k = \sqrt{\frac{2}{N+1}} \sum_{h=1}^N \sin(kh) c_h$ ,  $c_h = -\prod_{l=1}^{h-1} (\sigma_z^l) \sigma_-^h$  are canonical fermionic operators, and  $\psi_{kh}(t) = 2dt[\cos(k) + \cos(h)]$ , and we have assumed open boundary conditions on the chain. In order to characterize the evolution of the individual spin operators, we can express the evolved state  $\rho_j^{\text{DQ}}(t)$  in terms of the  $c_h$  operators. This yields:

$$\rho_j^{\text{DQ}}(t) = (-1)^{j-1} \left\{ \sum_{p-q \in \text{even}} (c_p^\dagger c_q + c_q^\dagger c_p) A_{j,q}(t) A_{j,p}(t) + \sum_{p-q \in \text{odd}} i^{p-q} (c_p^\dagger c_q^\dagger - c_q c_p) A_{j,q}(t) A_{j,p}(t) \right\}, \quad (5)$$

where the time-dependent amplitudes  $A_{j,q}$  read

$$A_{j,q}(t) = \sum_{m=0}^{\infty} i^{2m\tilde{N}} \left[ i^\delta J_{2m\tilde{N}+\delta}(2dt) - i^\Sigma J_{2m\tilde{N}+\Sigma}(2dt) \right] + \sum_{m=1}^{\infty} i^{2m\tilde{N}} \left[ i^{-\delta} J_{2m\tilde{N}-\delta}(2dt) - i^{-\Sigma} J_{2m\tilde{N}-\Sigma}(2dt) \right] \quad (6)$$

with  $\tilde{N} = N + 1$ ,  $\delta = q - j$ ,  $\Sigma = q + j$ , and  $J_n(\cdot)$  being the  $n$ -th order Bessel function of the first kind. Similarly, for a thermal initial state  $\rho_{\text{th}} = \mathbf{1} - \sum_j \sigma_j^z$ , we find the deviation density operator at time  $t$

$$\rho_{\text{th}}^{\text{DQ}}(t) = - \sum_{p-q \in \text{even}} (c_p^\dagger c_q + c_q^\dagger c_p) A_{p,q}(2t) + \sum_{p-q \in \text{odd}} (c_p^\dagger c_q^\dagger - c_q c_p) A_{p,q}(2t). \quad (7)$$

Taking the even/odd constraint into account, the density operators in Eqs. (5) and (7) are seen to belong to a  $N(N+1)/2$ -dimensional operator subspace which defines the Liouville space within which the transport occurs. Mapping back to spins, and assuming  $p \geq q$ , we get:

$$\begin{aligned} c_p^\dagger c_q^\dagger &= \sigma_q^+ \sigma_{q+1}^z \cdots \sigma_{p-1}^z \sigma_p^+, & c_q c_p &= \sigma_q^- \sigma_{q+1}^z \cdots \sigma_{p-1}^z \sigma_p^-, \\ c_q^\dagger c_p &= \sigma_q^+ \sigma_{q+1}^z \cdots \sigma_{p-1}^z \sigma_p^-, & c_q^\dagger c_q &= \frac{1}{2} (\mathbf{1} - \sigma_q^z). \end{aligned} \quad (8)$$

The above quadratic scaling is the same that Fel'dman and coworkers theoretically established for the XX Hamiltonian [50]†. While  $\rho_{\text{th}}$  is a constant of the motion under

† It is also interesting to observe that the operators in Eq. (8) are the same as the string operators in the spin-spin correlation functions  $S_{\text{XX}}(q, p)$  defined in T. S. Cubitt and J. I. Cirac, Phys. Rev. Lett. **100**, 180406 (2008).

the XX Hamiltonian, evolution of the end-polarized state can be readily expressed as

$$\rho_j^{\text{XX}}(t) = - \sum_{p,q} i^{p+q} (c_p^\dagger c_q + c_q^\dagger c_p) A_{j,q}(t) A_{j,p}(t). \quad (9)$$

### 3.2. Magnetization Dynamics and Transport Velocity

We can re-examine the experimental data in Figs. 1 and 2 using the analytical results outlined above. The magnitude of the collective spin magnetization is given by  $S(t) = \sum_{p=1}^N A_{1,p}^2(t)$  for an end-polarized initial state, and by  $S(t) = \sum_{p=1}^N A_{p,p}(2t)$  for a thermal initial state. The dashed black lines in the figures are the best fits to these expressions, where we have assumed that  $N$  is sufficiently large that no boundary effects are observed. Thus we only used the  $m = 0$  term in Eq. (6) to calculate  $A_{1,p}$  and  $A_{p,p}$  to calculate  $S(t)$  as shown above. For the end-polarized state we have also assumed that on the timescale of the experiment the magnetization propagating from the two ends have not had a chance to overlap, and we can thus describe them as two independent chains. This allows us to ignore the  $A_{N,p}$  term.

Three fitting parameters were used: a scalar multiplier, the frequency argument of the Bessel function, and an additive baseline constant. The baseline constant was subtracted from the data shown in the two figures, so that the oscillations are observed around zero. For the thermal initial state, the observed signal is seen to damp out at a faster rate than expected from the model. This is likely due to the presence of longer-range couplings that have been ignored in the NN model, as these long-range couplings lead to a leakage out of the restricted Liouville space. The obtained fitting frequencies yield  $d = 8.32 \times 10^3$  rad/s (8-pulse, thermal state),  $d = 8.52 \times 10^3$  rad/s (4-pulse, thermal state),  $d = 8.71 \times 10^3$  rad/s (8-pulse, end polarized state – see Appendix A), and  $d = 9.56 \times 10^3$  rad/s (4-pulse, end polarized state), yielding an estimate  $d = 8.78 \pm 0.55 \times 10^3$  rad/s. The estimate is biased by the value obtained in the 4-pulse experiment on the end-polarized state, where the fitting frequency is seen to be too high at longer times (Fig. 2). However, the estimate is still in good agreement with the values  $d = 8.3 \times 10^3$  rad/s, obtained from observing MQ coherences [40], and  $d = 8.17 \times 10^3$  rad/s, obtained from the known structure of FAp [38].

In the thermodynamic limit, the magnitude of the magnetization transported from site  $j = 1$  at time  $t = 0$  to site  $j = n$  at time  $t$  is given by  $P_{1,n}^\infty(t) = A_{1,n}^\infty(t)^2$ , where

$$A_{1,n}^\infty(t) = i^{n-1} \frac{n J_n(2dt)}{2dt} = i^{n-1} \frac{J_{n-1}(2dt) + J_{n+1}(2dt)}{2}. \quad (10)$$

Using properties of the Bessel functions [51], it is possible to show that  $\partial_t A_{1,n}^\infty = -d(A_{1,n+1}^\infty - A_{1,n-1}^\infty)$ . If we define a continuous spatial variable  $z = aj$ , with  $a$  equal to the distance between two spins and  $j$  being the spin number in the chain, we can replace the finite difference with a spatial derivative  $\partial_t A_{1,n}^\infty = -2ad\partial_z A_{1,n}^\infty$ . Taking the second derivative with respect to time we thus obtain a wave equation for the transport amplitude:

$$\partial_t^2 A_{1,n}^\infty = (2ad)^2 \partial_z^2 A_{1,n}^\infty. \quad (11)$$



$P_{1,n}^\infty(t)$  also follows the same wave equation with velocity  $2ad$ . We can also calculate the group velocity of the spin system directly from the dispersion relation for the DQ Hamiltonian,  $\omega(k) = 2d|\cos(ka)|$ , which results in  $v_g = \partial\omega/\partial k|_{k=\pi/2a} = 2ad$ . Using  $d = 8.78 \pm 0.55 \times 10^3$  rad/s, and  $a = 3.442$  Å, we obtain  $v_g \approx 6.04 \pm 0.38$  μm/s. This corresponds to a displacement of  $\approx 9.07 \pm 0.57$  nm in 1.5 ms or transport across  $N = 26 \pm 2$  spins. The time taken to travel a distance of  $n$  lattice sites is  $t = n/2d$ . At this time  $A_{1,n}^\infty = i^{n-1}J_n(n)$ , and  $P_{1,n}^\infty = (-1)^{n-1}J_n^2(n)$ . For large  $n$ ,  $J_n(n) \sim \frac{1}{\Gamma(2/3)} \left(\frac{2}{9n}\right)^{1/3}$  [51] and the magnitude of the polarization transported from spin 1 to  $n$  scales as

$$P_{1,n}^\infty(n) \sim n^{-2/3}. \quad (12)$$

### 3.3. Evolution of Multi-spin Correlations

Figure 3 shows the dynamics of the 1,2,3, and 4-spin correlations for a  $N = 9$  spin chain initialized in the state  $\rho_1 = \mathbf{1} - \sigma_z^1$ . These curves were generated using Eqs. (3) and (4). We can express  $A_{1,q}$  as

$$A_{1,q} = \sum_{m=0}^{\infty} i^{2m\tilde{N}+q-1} \left( \frac{2m\tilde{N}+q}{dt} \right) J_{2m\tilde{N}+q}(2dt) + \sum_{m=1}^{\infty} i^{2m\tilde{N}-q+1} \left( \frac{2m\tilde{N}-q}{dt} \right) J_{2m\tilde{N}-q}(2dt)$$

where we have used the Bessel function identity  $J_{\nu-1}(z) + J_{\nu+1}(z) = \frac{2\nu}{z}J_\nu(z)$  [51]. The sequential growth outlined above can easily be visualized in these simulations. The figures show that the presence of the boundary (at  $2dt_m \approx 5$ , where  $t_m \sim N/2d$  identifies the so-called ‘‘mirror time’’, see also next section) has a large effect on the spin dynamics. In Appendix B we show that additional insight into the dynamics is obtained by calculating the short-time evolution, and examining the growth of the multi-spin operators.

It is possible to experimentally characterize the growth of these multi-spin correlations. In a MQ experiment [43], we record the coherence orders by performing a collective rotation of the state about the  $z$ -axis, and observing the resulting phase shifts. The first row of Eq. (8) shows the double-quantum coherences created during NN DQ evolution, while the second row shows the zero-quantum coherences and the polarization states.

While we cannot directly observe the high-spin correlations in Eq. (8), we can use so-called  $x$ -basis encoding techniques to characterize the distribution of  $p - q$  [44], thereby indirectly probing the growth of these terms. For example, the first term in Eq. (8) in the  $x$ -basis reads:

$$c_p^\dagger c_q^\dagger = \left[ \sigma_q^x + \frac{i}{2}(\sigma_q^{x+} + \sigma_q^{x-}) \right] \frac{(\sigma_{q+1}^{x+} - \sigma_{q+1}^{x-}) \cdots (\sigma_{p-1}^{x+} - \sigma_{p-1}^{x-})}{(2i)^{p-q-2}} \left[ \sigma_p^x + \frac{i}{2}(\sigma_p^{x+} + \sigma_p^{x-}) \right],$$

where  $\sigma_q^{x\pm} = \sigma_q^y \pm i\sigma_q^z$  [52]. Here, a collective rotation of the system about the  $x$ -axis results in overlapping binomial distributions of phase factors whose highest order is  $p - q$ . Higher-order coherences in the  $x$ -basis are thus a signature of the presence of multi-spin correlations. Figure 4 shows the relative  $x$ -basis coherence intensities measured

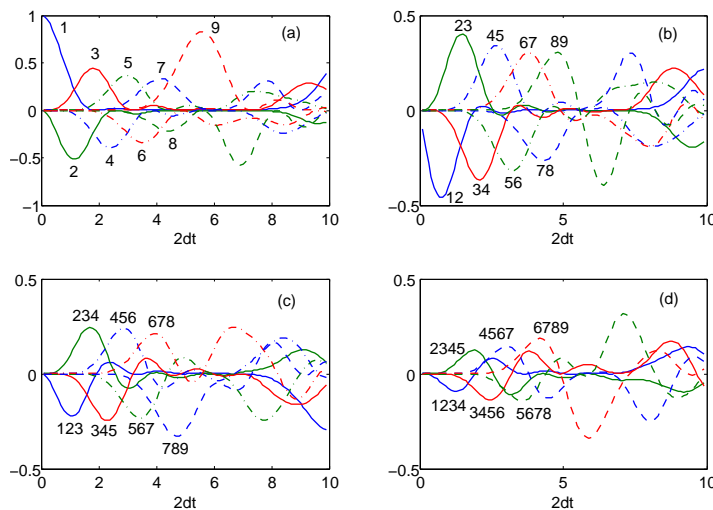


**Figure 3.** This figure illustrates the evolution of the 1,2,3, and 4-spin correlations for a  $N = 9$  spin system initialized in the state  $\rho_1 = \mathbf{1} - \sigma_1^z$ . The amplitudes of different product operators are obtained from Eqs. (3) and (4) in the main paper. (a) Single spin polarization terms  $\sigma_n^z$ . The amplitudes are given by  $A_{1,n}^2(t)$ . (b) Two spin correlation terms  $h_{n,n+1}^{(2)}$ . These are double quantum terms whose amplitudes are given by  $A_{1,n}(t)A_{1,n+1}(t)$ . (c) Three spin correlation terms  $h_{n,n+1,n+2}^{(3)}$ . These are zero quantum terms whose amplitudes are given by  $A_{1,n}(t)A_{1,n+2}(t)$ . (d) Four spin correlation terms  $h_{n,n+1,n+2,n+3}^{(4)}$ . These are double quantum terms whose amplitudes are given by  $A_{1,n}(t)A_{1,n+3}(t)$ . Higher order correlations are not shown.

as a function of the DQ evolution time, starting from the end-polarized state. The experiments were performed using a 16-pulse implementation of the DQ Hamiltonian [44], and both the number of cycles and the delay  $\Delta$  were varied. It can be seen that following an initial rapid creation of 3-spin correlations (and concomitant reduction in the single spin term), the coherence orders change quite slowly.

### 3.4. Mirror Times

Equations (3)–(7) also help us understand the source of the signal enhancements observed near the boundaries of a finite spin chain. The sum over  $m$  in Eq. (6) resembles a sum over an infinite number of copies of the  $N$ -spin chain (consistent with the periodic boundary conditions imposed by the sine transform [49]). At short times, only the lower-order Bessel functions contribute, and each “replica” of the chain is independent of the others. At longer times, the adjacent copies begin to interfere with each other as illustrated in Fig. 5. It is the interference between these terms that is responsible for the *mirror times* observed in our previous work [40], consistent with the interpretation in terms of bouncing spin-wave packets and “erratic” dynamics put forward for the XX model [50]. In particular, the leading mirror term yields a factor of 4 increase in the magnitude of the transferred magnetization. A similar transport behavior has been shown for pure states [53].

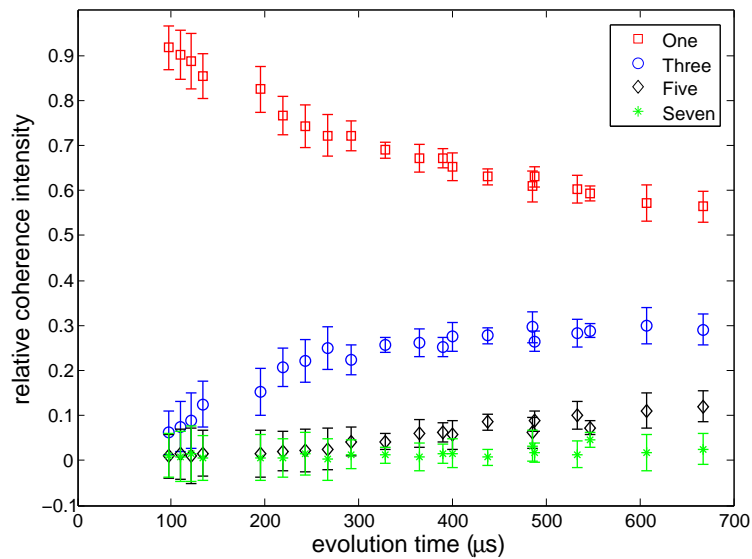


**Figure 4.** Growth of  $x$ -basis coherences during DQ evolution, starting from an end-polarized initial state. Only odd-order coherences are observed due to selection rules.

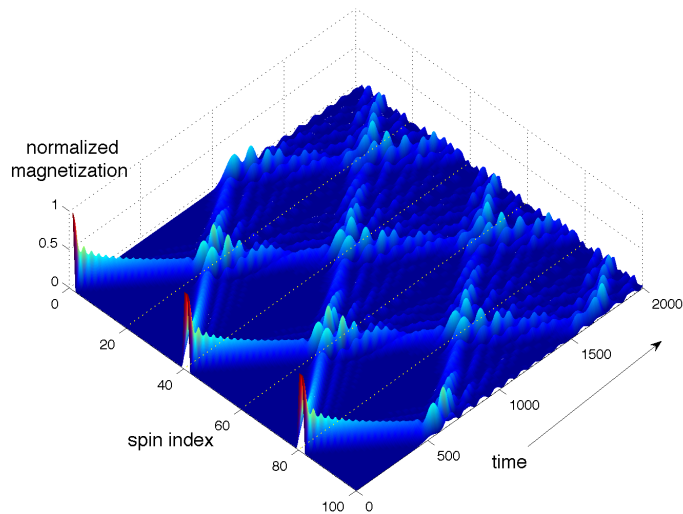


**Figure 5.** Five copies of a 20-spin chain illustrate the origin of the interference patterns observed following reflection off the boundary during evolution under the NN XX Hamiltonian. The time axis is in units of  $1/d$ .

Fig. 6 shows that the mirror enhancements obtained under the DQ Hamiltonian are also due to interferences generated as a polarization wave-packet reflects off the boundary in a finite spin chain. In the case of the DQ Hamiltonian the polarization is inverted at every adjacent spin site as it travels down the chain, and the nature of interferences at the boundary depends on whether the chain contains an even or odd number of spins.

The above mirror dependence on chain length is also manifested in the multiple quantum coherence dynamics of the spin chain. Mirror times were also observed in the

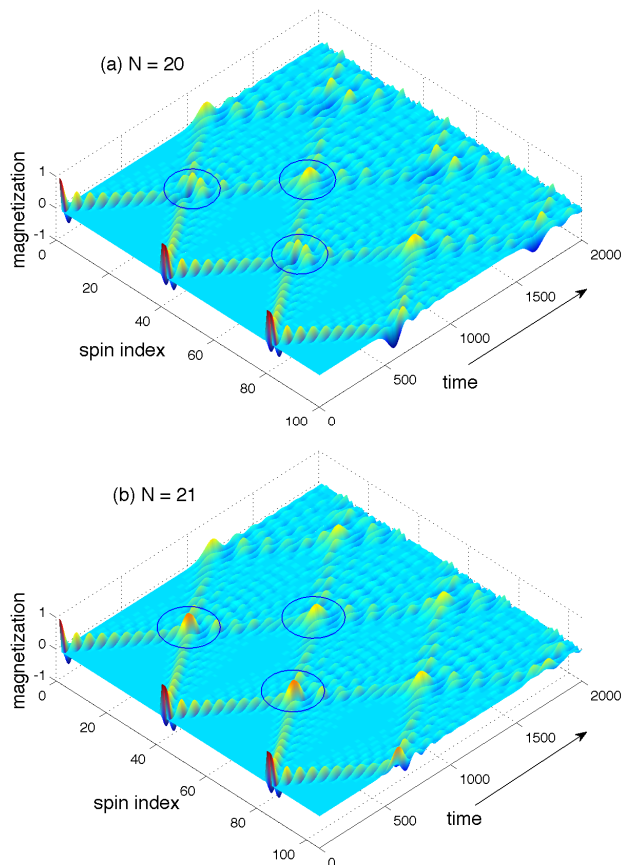


**Figure 6.** Five copies of a spin chain illustrating the boundary interferences for (a)  $N = 20$ ; (b)  $N = 21$  during evolution under the NN DQ Hamiltonian. The time axis is in units of  $1/d$ .

multiple quantum dynamics for thermally polarized spin chains [40]. We can explain this as follows. Although significant overlap for waves originating at symmetric spin positions  $j$  and  $N + 1 - j$  can occur at different times depending on  $j$  (for example, at times  $t_j \propto N \pm j$ ) there is also large overlap at the time  $t_m \propto N$ , when one of the waves has bounced off a boundary and encounters the second wave originating from the symmetric spin (see Fig. 7). Since at each time  $t_j$  there occurs only the overlap for one pair, weighted by a factor  $N$ , only the overlaps at the mirror time  $t_m \propto N$  are noticeable for the thermal initial state [40].

#### 4. Summary

In summary, we have measured the single-spin and two-spin Liouville-space operators that drive the (nearly) ballistic transport of magnetization under the DQ Hamiltonian at room temperature. We also developed a real-space description of the spin dynamics that is able to accurately describe the observed results, by allowing us to characterize the growth and coherent dynamics of multi-spin correlations, and to explain the origin

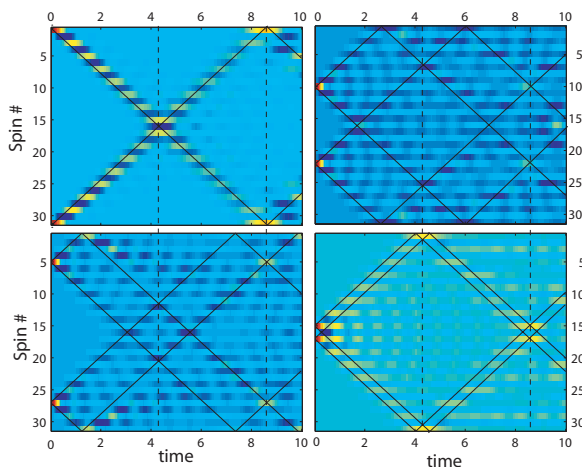


**Figure 7.** Zero quantum coherence intensities  $J_{j,l}^0(t) + J_{N+1-j,l}^0(t)$  as a function of time in a chain of  $N = 31$  spins. Left top:  $j = 1$ ; Left bottom:  $j = 5$ ; Right top:  $j = 10$ ; Right bottom:  $j = 15$ . The black lines are drawn as a guide for the eye.

of the previously described “mirror times” in finite spin chains. Within the validity of a NN approximation, the dynamics of the  $N$ -spin system are seen to be restricted to a Liouville space whose size grows only quadratically with  $N$ . Based on our model, we estimate that the magnetization is coherently transported down the chain with a group velocity of  $6.04 \pm 0.38 \mu\text{m/s}$ . We expect this velocity to be directly independently measurable using reciprocal space NMR methods [54].

## Acknowledgments

This work was funded in part by the NSA under ARO contract number W911NF0510469 and the NSF under Awards 0702295, DMR-1005926 (to PC) and PHY-0903727 (to LV). DGC acknowledges support from the Canadian Excellence Research Chairs (CERC) program. The FAp crystal used in the experiments was grown by Prof. Ian Fisher.

## Appendix A. Evolution of the end-polarized state under $\mathcal{H}_{\text{DQ}}$

Figure A1 shows the experimental results obtained using the 8-pulse implementation of the DQ Hamiltonian (in contrast to the 4-pulse version shown in Figure 2), when the spins are prepared in the end-polarized state  $\rho_{1N} \approx \mathbf{1} - \epsilon(\sigma_1^z + \sigma_N^z)$  in which the polarization is localized at the ends of the chain. Fitting the magnetization dynamics to the analytical model results in a value of  $d = 8.7 \times 10^3 \text{ rad/s}$ .

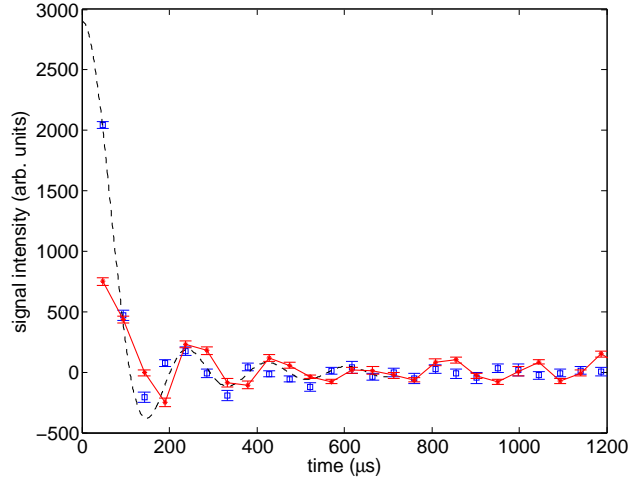


**Figure A1.** Evolution of the end-polarized initial state under  $\mathcal{H}_{\text{DQ}}$ , showing the collective magnetization ( $\sum_i \sigma_z^i$  — blue squares) and the two-spin correlations ( $\sum_i (\sigma_x^i \sigma_y^{i+1} + \sigma_y^i \sigma_x^{i+1})$  — red asterisks). The dashed black line is the best fit of the observed magnetization to the analytical model described later (yielding  $d = 8.7 \times 10^3$  rad/s). The solid red line connecting the red asterisks is a guide to the eye.

## Appendix B. Short time evolution

Let the initial state of the spin system be  $\rho_j = \mathbf{1} - \sigma_z^j$ . The state of the spin system at a time  $t$  later, following evolution under the DQ Hamiltonian is

$$\rho_t = \rho_0 - it [\mathcal{H}_{\text{DQ}}, \rho_0] - \frac{t^2}{2} [\mathcal{H}_{\text{DQ}}, [\mathcal{H}_{\text{DQ}}, \rho_0]] - \frac{it^3}{6} [\mathcal{H}_{\text{DQ}}, [\mathcal{H}_{\text{DQ}}, [\mathcal{H}_{\text{DQ}}, \rho_0]]] + \dots \quad (\text{B.1})$$

Evaluating the above commutators, we get

$$[\mathcal{H}_{\text{DQ}}, \rho_0] = 2d \left( h_{j-1,j}^{(2)} + h_{j,j+1}^{(2)} \right), \quad (\text{B.2})$$

where  $h_{i,j}^{(2)} = \sigma_i^+ \sigma_j^+ - \sigma_i^- \sigma_j^- = \frac{i}{2} (\sigma_i^x \sigma_j^y + \sigma_i^y \sigma_j^x)$ . A collective rotation of  $h_{i,j}^{(2)}$  about the  $z$ -axis by an angle  $\phi$  results in phase shifts by angles  $\pm 2\phi$ , indicating a double quantum coherence. Similarly,

$$[\mathcal{H}_{\text{DQ}}, [\mathcal{H}_{\text{DQ}}, \rho_0]] = -2d^2 \left( \sigma_{j-1}^z + 2\sigma_j^z + \sigma_{j+1}^z \right) - 2d^2 \left( h_{j-2,j-1,j}^{(3)} + 2h_{j-1,j,j+1}^{(3)} + h_{j,j+1,j+2}^{(3)} \right), \quad (\text{B.3})$$

where  $h_{i,j,k}^{(3)} = \sigma_i^+ \sigma_j^z \sigma_k^- + \sigma_i^- \sigma_j^z \sigma_k^+$  and

$$[\mathcal{H}_{\text{DQ}}, [\mathcal{H}_{\text{DQ}}, [\mathcal{H}_{\text{DQ}}, \rho_0]]] = 6d^3 \left( h_{j-2,j-1}^{(2)} + 3h_{j-1,j}^{(2)} + 3h_{j,j+1}^{(2)} + h_{j+1,j+2}^{(2)} \right) - 2d^3 \left( h_{j-3,j-2,j-1,j}^{(4)} + 3h_{j-2,j-1,j,j+1}^{(4)} + 3h_{j-1,j,j+1,j+2}^{(4)} + h_{j,j+1,j+2,j+3}^{(4)} \right), \quad (\text{B.4})$$

where  $h_{i,j,k,l}^{(4)} = \sigma_i^+ \sigma_j^z \sigma_k^z \sigma_l^+ + \sigma_i^- \sigma_j^z \sigma_k^z \sigma_l^-$ , and so on. Collective rotations of  $h_{i,j,k}^{(3)}$  and  $h_{i,j,k,l}^{(4)}$  about the  $z$ -axis by an angle  $\phi$  results in phase shifts by angles 0 and  $\pm 2\phi$  respectively, indicating these are zero and double quantum coherences. We observe the same alternating zero and double-quantum signatures in the commutator expansion

as obtained in the fermionic solution (Eq. (3) in the main text). Moreover, here we see that the growth of the spin system is necessarily slow. At the level of the second commutator, we can infer that the system is 3 times more likely to evolve from a 3-spin state to a 2-spin state, than it is to evolve to a 4-spin state. This is one indication of why locally polarized states are transported almost ballistically along the spin chain. This is schematically illustrated in Fig. B1.

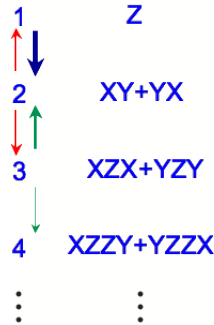


**Figure B1.** The successive commutators in Eqs. B1–B4 yield the Liouville space operators shown in the figure and illustrate the progressive generation of zero and double quantum coherences.

## References

- [1] G. Roumpos, C. P. Master, Y. Yamamoto, *Phys. Rev. B* **75**, 094415 (2007).
- [2] I. Buluta, F. Nori, *Science* **326**, 108 (2009), and references therein.
- [3] T. Giamarchi, *Quantum Physics in One Dimension* (Oxford, 2004).
- [4] S. Bose, *Phys. Rev. Lett.* **91**, 207901 (2003).
- [5] M. Friesen, A. Biswas, X. Hu, D. A. Lidar, *Phys. Rev. Lett.* **98**, 230503 (2007).
- [6] F. Meier, D. Loss, *Phys. Rev. Lett.* **90**, 167204 (2003).
- [7] E. Lieb, T. Schultz, D. Mattis, *Ann. Phys.* **16**, 407 (1961).
- [8] V. E. Korepin, N. M. Bogoliubov, A. G. Izergin, *Quantum Inverse Scattering Method and Correlation Functions* (Cambridge, Cambridge UK, 1997).
- [9] D. C. Mattis, *The Theory of Magnetism Made Simple* (World Scientific, Singapore, 2006).
- [10] A. Kay, *Int. J. Quantum Inf.* **8**, 641 (2010), and references therein.
- [11] J. Sirker, R. G. Pereira, I. Affleck, *Phys. Rev. Lett.* **103**, 216602 (2009).
- [12] M. Esposito, P. Gaspard, *Phys. Rev. B* **71**, 214302 (2005).
- [13] M. Znidaric, *J. Stat. Mech.* (2010) L05002.
- [14] V. Eisler, *J. Stat. Mech.* P06007 (2011).
- [15] S. Mukerjee and B. Sriram Shastry, *Phys. Rev. B* **77**, 245131 (2008).
- [16] F. Heidrich-Meisner, A. Honecker, D. C. Cabra, and W. Brenig, *Phys. Rev. Lett.* **92**, 069703 (2004).
- [17] L. F. Santos, *J. Math. Phys.* **50**, 095211 (2009).
- [18] H. Cho, T. D. Ladd, J. Baugh, D. G. Cory, C. Ramanathan, *Phys. Rev. B* **72**, 054427 (2005).
- [19] G. A. Alvarez and D. Suter *Phys. Rev. Lett.* **104**, 230403 (2010).
- [20] M. A. Cazalilla and M. Rigol, *New J. Phys.* **12**, 055006 (2010), Focus Issue.
- [21] R. Bruschweiler and R. R. Ernst, *Chem. Phys. Lett.* **264**, 393 (1997).
- [22] J. S. Waugh, *Mol. Phys.* **95**, 731 (1998).
- [23] S. W. Morgan, B. V. Fine, B. Saam, *Phys. Rev. Lett.* **101**, 067601 (2008).

- [24] W. Zhang, D. G. Cory, Phys. Rev. Lett. **80**, 1324 (1998).
- [25] G. S. Boutis, D. Greenbaum, H. Cho, D. G. Cory, C. Ramanathan, Phys. Rev. Lett. **92**, 137201 (2004).
- [26] S. Zhang, B. H. Meier, R. R. Ernst, Phys. Rev. Lett. **69**, 2149 (1992).
- [27] P. R. Levstein, G. Usaj, H. M. Pastawski, *J. Chem. Phys.* **108**, 2718 (1998).
- [28] H. M. Pastawski, P. R. Levstein, G. Usaj, J. Raya, J. Hirschinger, *Physica* **283**, 166 (2000).
- [29] P. Cappellaro, L. Viola, C. Ramanathan, Phys. Rev. A **83**, 032304 (2011).
- [30] F. J. Ruess, W. Pok, T. C. Reusch, M. Butcher, K. E. Goh, L. Oberbeck, G. Scappucci, A. Hamilton, and M. Simmons Small **3**, 563 (2007),
- [31] Z. M. Wang, K. Holmes, Y. I. Mazur, and G. J. Salamo, Applied Physics Letters **84**, 1931 (2004)
- [32] G. M. Nikolopoulos, D. Petrosyan, and P. Lambropoulos Journal of Physics: Condensed Matter **16**, 4991 (2004)
- [33] Petit, P. and Spegt, P. J. Phys. France **51**, 1645 (1990)
- [34] J. R. Weber, W. F. Koehl, J. B. Varley, A. Janotti, B. B. Buckley, C. G. Van de Walle, and D. D. Awschalom PNAS **107**, 8513 (2010),
- [35] J. Wrachtrup PNAS **107**, 9479 (2010)
- [36] M. Engelsberg, I. J. Lowe and J. L. Carolan, Phys. Rev. B **7**, 924 (1973).
- [37] G. Cho and J. P. Yesinowski, Chem. Phys. Lett. **205**, 1 (1993).
- [38] G. Cho and J. P. Yesinowski, J. Phys. Chem. **100**, 15716 (1996).
- [39] E. Rufeil-Fiori, C. M. Sanchez, F. Y. Oliva, H. M. Pastawski, P. R. Levstein, Phys. Rev. A **79**, 032324 (2009).
- [40] W. Zhang, P. Cappellaro, N. Antler, B. Pepper, D. G. Cory, V. V. Dobrovitski, C. Ramanathan, L. Viola, Phys. Rev. A **80**, 052323 (2009).
- [41] C. P. Slichter, *Principles of Magnetic Resonance* (Springer, New York, 1996).
- [42] L. Emsley and A. Pines, "Lectures on Pulsed NMR (2nd Ed.)," in Nuclear Magnetic Double Resonance, Proceedings of the CXXIII School of Physics "Enrico Fermi," World Scientific, Amsterdam (1993).
- [43] Y.-S. Yen, A. Pines, J. Chem. Phys. **78**, 3579 (1983).
- [44] C. Ramanathan, H. Cho, P. Cappellaro, G. S. Boutis, D. G. Cory, Chem. Phys. Lett. **369**, 311 (2003).
- [45] U. Haeberlen, *High resolution NMR in solids: Selective averaging* (Academic Press, New York, 1976).
- [46] C. Ramanathan, S. Sinha, J. Baugh, T. F. Havel, D. G. Cory, Phys. Rev. A **71**, 020303 (2005).
- [47] P. Cappellaro, C. Ramanathan, D. G. Cory, Phys. Rev. A **76**, 032317 (2007a).
- [48] E. B. Fel'dman S. Lacelle, J. Chem. Phys. **107**, 7067 (1997).
- [49] P. Cappellaro, C. Ramanathan, D. G. Cory, Phys. Rev. Lett. **99**, 250506 (2007b).
- [50] E. B. Fel'dman, R. Bruschiweiler, R. R. Ernst, Chem. Phys. Lett. **294**, 297 (1998).
- [51] M. Abramowitz and I. A. Stegun, eds., *Handbook of Mathematical Functions* (Dover, New York, 1972).
- [52] Y. Zhang, W. E. Maas, D. G. Cory, Mol. Phys. **86**, 347 (1995).
- [53] L. Banchi, T. J. G. Apollaro, A. Cuccoli, R. Vaia, P. Verrucchi, Phys. Rev. A **82**, 052321 (2010)
- [54] A. Sodickson, D. G. Cory, Prog. Nucl. Mag. Reson. Sp. **33**, 77 (1998).